Collective magnetism of a single-crystalline nanocomposite FeCoCrMnAl high-entropy alloy

A. Jelen [a], P. Koželj [a,b], D. Gačnik [a], S. Vrtnik [a], M. Krnel [a], G. Dražić [c], M. Wencka [d], Z. Jagličić [e,f], M. Feuerbacher [g,§], J. Dolinšek [a,b,*]

[a] *Jožef Stefan Institute, Jamova 39, SI-1000 Ljubljana, Slovenia*

[b] *University of Ljubljana, Faculty of Mathematics and Physics, Jadranska 19, SI-1000 Ljubljana, Slovenia*

[c] *National Institute of Chemistry, Department of Materials Chemistry, Hajdrihova 19, SI-1000 Ljubljana, Slovenia*

[d] *Institute of Molecular Physics, Polish Academy of Sciences, Smoluchowskiego 17, PL-60-179 Poznań, Poland*

[e] *Institute of Mathematics, Physics and Mechanics, Jadranska 19, SI-1000 Ljubljana, Slovenia*

[f] *University of Ljubljana, Faculty of Civil and Geodetic Engineering, Jamova 2, SI-1000 Ljubljana, Slovenia*

[g] *Institut für Mikrostrukturforschung, Forschungszentrum Jülich, D-52425 Jülich, Germany*

* Corresponding author. *E-mail address*: jani.dolinsek@ijs.si (J. Dolinšek).

§ Corresponding author. *E-mail address:* m.feuerbacher@fz-juelich.de (M. Feuerbacher)

Abstract

We have investigated the nature of the magnetic state of a single-crystalline FeCoCrMnAl nanocomposite high-entropy alloy (HEA), composed of crystallographically oriented magnetic nanoplatelets embedded in a magnetic matrix of different magnetic order. The two-phase nanocomposite was formed by a bcc-B2 spinodal decomposition. Due to the single-crystalline nature of the material, there is no symmetry breaking of the surface atomic monolayer at the borders between the two phases and there are no interface regions between the nanoplatelets and the matrix. The material also does not exhibit grain structure, allowing for the observation of the true intrinsic magnetism of a nanocomposite HEA. Upon cooling, the predominantly Fe-Cr-Mn chemically disordered bcc matrix orders first at $T_{C1} \approx 425$ K in an asperomagnetic-type magnetic state. Below $T_{C2} \approx 370$ K, the B2 nanoplatelets that are predominantly an $Al_{30}(Co,Mn)_{70}$ pseudo-binary intermetallic compound, start to order in a ferromagnetic (FM)-type manner. We have focused to the question whether the magnetic state of the nanocomposite below T_{C2} is a collective state of the interacting nanoplatelets and the matrix or their coupling is weak enough that the magnetic ordering of each of them can be treated independently. Experimental results support the development of a single collective, disordered FM-type magnetic state upon cooling due to the exchange coupling between the nanoplatelets and the matrix. The nanocomposite is magnetically soft and the strong variation of the magnetization with the temperature in a large interval $\Delta T \approx$ 125 K just above room temperature due to two successive magnetic phase transitions make this material promising for the application in magnetocaloric refrigeration.

Keywords: high-entropy alloys; nanostructured materials; magnetic properties.

1. Introduction

A characteristic feature of nanoscale magnets is at least one dimension in the nanometer range (1 – 100 nm) [1]. When the small dimension becomes comparable to a characteristic magnetic or electrical length scale, nanomagnets exhibit size-specific magnetic properties such as superparamagnetism, remanence enhancement, exchange averaging of magnetic anisotropy (leading to a magnetically soft material) or giant magnetoresistance. Examples of characteristic length scales are the domain wall width δ_w, the exchange length l_{ex} (the balance of exchange and dipolar interactions) and the dimensionless magnetic hardness parameter (the ratio of anisotropy to dipole energy). The number of small dimensions in a nanoscale magnet can be one (magnetic thin films that form the basis of modern magnetic sensors and memory elements), two (magnetic nanowires and nanoneedles) or three (magnetic nanoparticles). These magnetic nano-objects can be separated or embedded in a matrix (either nonmagnetic or magnetic) to form a nanocomposite.

A general feature of nanostructures is a large portion of surface or interface atoms [1]. In a film, wire or particle of 10 nm dimension, the fraction of surface atoms reaches 5, 10 or 15 %, respectively. These surface atoms, together with the reduced dimensions are at the origin of altered magnetic properties of a nanostructured material. The surface monolayer exhibits broken symmetry, which then extends to the first few monolayers beneath due to structural relaxation normal to the surface. The broken symmetry introduces strains, modifies the magnetic anisotropy and frustrates the exchange and dipolar couplings within the interface region and its neighborhood.

High-entropy alloys (HEAs) are multicomponent equiatomic or near-equiatomic alloys, which form mostly solid solutions including random solid solutions and partially ordered ones. The concept of high entropy introduces a new strategy of developing advanced materials with

promising properties like high wear resistance, corrosion resistance, high strength, high fracture toughness and plastic deformation [2-5]. HEAs composed of 3*d*, 4*d* and 5*d* transition elements, sometimes alloyed with additional elements like Al, B and Si, belong to the class of "regular" solutions, where the interactions between unlike atomic kinds are different from those between like atoms, yielding nonzero mixing enthalpy, $\Delta H_{mix} \neq 0$. In such HEAs, random mixing of the elements on the crystal lattice is compromised and preferential chemical environments are formed on a nanometric scale [6,7], which is more pronounced in thermally annealed materials. Nonrandom mixing of the elements is also favored by the atomic size differences [8,9], where clustering of the atoms of similar size minimizes the lattice distortion in a given nanoscale volume, which reduces the lattice strain energy and hence ΔH_{mix}. In regular solutions, positive ΔH_{mix} causes incomplete miscibility of the elements and leads to phase segregation, whereas negative ΔH_{mix} leads to the formation of intermetallic compounds. Regular HEAs are frequently structurally heterogeneous, showing in some cases a microstructure of more than one solid solution, a coexistence of a solid solution with an intermetallic compound, dendritic structure, precipitation and eutectic or spinodal decomposition.

In this paper, we report on the magnetism of a single-crystalline FeCoCrMnAl HEA (in the following abbreviated as FCCMA) that is an excellent nanocomposite magnet, composed of crystallographically oriented magnetic nanoplatelets embedded in a magnetic matrix of different magnetic order. Due to perfectly coherent phase boundaries, there is no symmetry breaking of the surface atomic monolayer at the borders between the two phases. Consequently, there are no interface regions between the nanoplatelets and the matrix and the material also does not exhibit grain structure. Under these conditions, the true intrinsic magnetism of a nanocomposite HEA is observed experimentally. We have focused to the question on the nature of the magnetic state of

the nanocomposite with the aim to find out whether or not there exists a single, collective magnetic state of the interacting nanoplatelets and the matrix, or their coupling is so weak that the magnetic ordering of each of them is independent.

2. Results

2.1. Material characterization

The FeCoCrMnAl single crystal used in this study was the same as the one reported in a recent publication [10], where the details of its preparation by the Bridgman technique are described. The volume of the primary grain was as large as 4.8 cm^3, enabling us to prepare single-crystalline samples of an appropriate size to measure the magnetic properties. The overall composition of the crystal was $Fe_{21.1}Co_{20.3}Cr_{21.1}Mn_{15.4}Al_{22.0}$. TEM micrographs [10] have shown that the material possesses a microstructure consisting of B2 inclusions in a bcc matrix, both occupying approximately equal volume fractions. The two-phase structure was formed by a bcc-B2 spinodal decomposition. The inclusions are $\{001\}$ nanoplatelets of about 65 nm thickness, with variable lateral extensions of the order of 500 nm. The microstructure of B2 inclusions (bright) in a bcc matrix (dark) is also evident from the SEM low-voltage secondary electron (SE) image of Fig. 1 (the contrast is discussed in the Appendix A). The three-dimensional platelet-type morphology of the inclusions is confirmed by Fig. B1 of the Appendix B, where the primary and the perpendicular surfaces are shown. Both surfaces were prepared by cutting and polishing with a gallium ion beam in an FIB instrument. A similar spinodally decomposed two-phase structure was found in

equiatomic AlCoCrFeNi HEA [11], however with the matrix/inclusion setting inverted to that of our FCCMA (the matrix is B2-ordered, whereas the inclusions are bcc).

High-resolution HAADF STEM images [10] have demonstrated that the phase boundaries between the bcc and the B2 phase are perfectly coherent. The lattice parameters of the bcc and the B2 phases according to STEM are the same (2.9 Å). All lattice planes pass through a phase boundary without any disturbance, so that the lattices of the two phases are aligned and in perfect registry. The SAED patterns originating from a volume containing the bcc and the B2 phases, as well as several phase boundaries, display only a single set of reflections and are undistorted and sharp [10]. These results reveal that the entire primary grain contains a single consistent and continuous set of lattice planes, and can be referred to as a single crystal (in the topological sense), even though two phases of different chemistry and order are present. The Bridgman technique employed is a near-equilibrium growth method. The applied growth velocity was low (5 mm/h) and the crystal was cooled very slowly, so that the solidified material was thermally annealed for several hours. The material is thus well equilibrated, so that the bcc-B2 two-phase nanostructure can be considered as thermodynamically stable and the chemical short-range ordering of the elements on the atomic scale has established.

The chemical compositions of the bcc matrix and the B2 inclusions on the nanometric scale were analyzed by STEM and EDS. A HAADF image of an area 300×300 nm^2 is shown in Fig. 2, together with the EDS elemental maps. In the HAADF STEM micrograph, the matrix appears bright and the inclusions are dark due to difference in the average atomic number (*Z*-contrast). The inclusions are Al-Co rich, containing also a significant fraction of Mn, whereas the matrix is predominantly Fe-Cr-Mn. The EDS line profile over the two phases is shown in Fig. 3. The average composition of the bcc matrix (in at. %) is $Fe_{28}Co_7Cr_{34}Mn_{25}Al_6$, whereas the average composition

of the B2 inclusions is $Fe_{14}Co_{39}Cr_7Mn_{17}Al_{23}$. The concentration of each element within each of the two phases fluctuates more or less randomly over the line profile by up to ±4 %, revealing that the matrix and the inclusions are compositionally inhomogeneous already by themselves on a 10-nm scale, presumably due to chemical short-range ordering.

The chemical compositions of the spinodally decomposed bcc and B2 phases can be qualitatively understood by considering binary mixing enthalpies ΔH_{mix}^{ij} of the constituent elements [12] (Table 1). For the Fe, Co, Cr and Mn, the enthalpies ΔH_{mix}^{ij} are all small (between 0 and –5 kJmol^{-1}), so that these elements mix well and produce a chemically disordered bcc solid solution. Aluminum possesses large negative mixing enthalpies with these transition elements (between –10 and –19 kJmol^{-1}), showing strong tendency to form intermetallic compounds. The largest negative binary mixing enthalpies are for the Al-Co and Al-Mn pairs, both amounting to –19 kJmol^{-1}, so that an Al-(Co,Mn) pseudo-binary intermetallic compound in a B2 structure (a chemically ordered bcc) is predominantly formed.

2.2. Magnetic measurements

The temperature dependent direct current (dc) zero-field-cooled (zfc) and field-cooled (fc) magnetizations in a magnetic field $B = 10$ mT are shown in Fig. 4. Upon cooling, a two-step magnetic phase transition is evident, the upper one occurring at $T_{C1} \approx 425$ K and the lower one at $T_{C2} \approx 370$ K, with both transitions resembling a FM-type. Below 300 K, a difference between M_{zfc} and M_{fc} starts to be observed. While M_{fc} saturates to a constant plateau, M_{zfc} slightly decreases upon cooling.

The two-step magnetic phase transition was further investigated by measuring the alternating current (ac) magnetic susceptibility, employing a magnetic field of amplitude $B_0 = 0.2$ mT and logarithmically spaced frequencies $\nu = 1$, 10, 100 and 1000 Hz. The real part of the ac susceptibility χ' in the temperature range 300 – 500 K is presented in Fig. 5a. At about 425 K, a peak is observed that shifts with an increasing frequency to higher temperatures (shown expanded in Fig. 5b). Such behavior is typical of a spin freezing transition in magnetically frustrated systems like spin glasses, disordered magnets and superparamagnets below the blocking temperature. By associating the temperature of the peak with the spin freezing temperature $T_f(\nu)$, the $T_f(\nu)/T_f(1\text{ Hz})$ relation is presented in the inset of Fig. 5b. A logarithmic dependence of T_f on the frequency is evident. The fractional shift of the freezing temperature per decade of frequency was evaluated to be $\Gamma = \Delta T_f/T_f \Delta(\log\nu) = 3\times10^{-4}$, which is in the range typically found in disordered magnets with competing FM and antiferromagnetic (AFM) interactions (for canonical spin glasses, larger values $\Gamma \approx 10^{-2} – 10^{-3}$ are typical) [13]. Below 370 K (Fig. 5a), χ' first rapidly increases upon cooling and then shows a tendency to saturate towards a temperature-independent plateau. Since the dc magnetization of Fig. 4 shows identical behavior in this temperature range, the increased amplitude of the ac magnetization follows the increase of the dc magnetization.

The magnetization versus the magnetic field curves, $M(H)$, were measured between $T_{C1} =$ 425 K and 2 K for a magnetic field sweep of ±7 T. A selected set of curves is shown in Fig. 6a, where a continuous evolution of their shape with the temperature upon cooling can be noticed. Just below T_{C1}, the FM-type curves saturate to an inclined linear line at high fields. Upon lowering the temperature, the magnetization grows, the shape of the $M(H)$ curves evolves toward a rectangular step at $H = 0$, and the inclination of the saturation line decreases until it vanishes below 100 K (the saturation plateau becomes horizontal). The decrease of the inclination of the saturation line

upon cooling is demonstrated on an expanded scale in the inset of Fig. 6a, where the parts of the $M(H)$ curves in the high-field range 4–7 T, normalized to their values at 7 T, $M(H)/M(7\text{ T})$, are shown. The $M(H)$ curves are magnetically soft at all temperatures. Due to the inherent hysteresis of the employed superconducting magnet, which is up to 1 mT, the width of the hysteresis loops of the FCCMA sample and the associated coercive field H_c were determined by using a palladium standard to subtract the magnet hysteresis. This procedure gives valid result once the coercive field of the sample is larger than the magnet hysteresis. For the FCCMA, this happens below 300 K. In Fig. 6b, we show the hysteresis curves at 100 K and 2 K on an expanded scale. The curves close up in the field of about $\mu_0 H \approx 40$ mT, revealing their FM-type character. The coercive field $\mu_0 H_c$ between 300 and 2 K is shown in the inset of Fig. 6b. Within that temperature range, the coercive field increases linearly from about 0.5 mT at 300 K to 4.3 mT at 2 K, revealing good soft magnetic characteristics of the FCCMA nanocomposite.

The nature of the magnetic state was further investigated by the thermoremanent magnetization (TRM) time-decay [14,15]. In a TRM experiment, the sample is cooled in a field H_{fc} to the measuring temperature T_m, where the cooling is stopped and the spin system is let to age isothermally for a waiting (aging) time t_w. After t_w, the field is cut to zero and the time decay of the magnetization is monitored over macroscopic times. Upon $H_{fc} \to 0$, the reversible part of the fc magnetization M_{fc} decays to zero almost instantaneously, whereas the irreversible part (the TRM) decays in time logarithmically slow. In magnetically frustrated systems, the TRM is a fraction of M_{fc} prior to cutting H_{fc} to zero. Its magnitude varies with the temperature from a few percent at higher temperatures up to the full M_{fc} upon $T \to 0$. The M_{TRM} time-decay depends on the aging temperature T_m, the aging time t_w and the cooling field H_{fc}. TRM is a measure of "stiffness" of the spin system, related to the length scale of the site-averaged spin correlations

$\langle \vec{S}_i(0) \cdot \vec{S}_j(r) \rangle$. This spatial correlation function defines the distance over which the spin correlations average to zero, depending on the strength of the interspin interactions. For the spin correlations that rapidly average to zero already at short distances (over a couple of interatomic spacing), the TRM is vanishing small, whereas longer spin correlations on a mesoscopic scale yield large, slowly decaying TRM.

We have measured the TRM decays at a set of temperatures T_m between 425 and 2 K. The sample was always cooled from RT to T_m in a field $\mu_0 H_{fc} = 10$ mT, and the waiting time $t_w = 1$ h was employed. Cutting the field to zero was accomplished in about 10 seconds and the TRM decay was then monitored over the time t of 3 h. The TRM amplitude at $t = 0$, normalized to the fc magnetization prior to cutting the field to zero, $M_{TRM}(0)/M_{fc}$, is shown in Fig. 7a. Its rather complicated temperature dependence will be discussed later. The normalized $M_{TRM}(t)/M_{TRM}(0)$ time-decay curves at a selected set of the measuring temperatures T_m are shown in Fig. 7b. The logarithmic decay is fast just below T_{C1} and then continuously slows down upon cooling, until it becomes unobservable below 200 K within the employed 3-h time window (the TRM is constant in time).

2.3. Magnetoresistance

Electrical resistivity ρ is another suitable quantity to characterize the magnetic state of a metallic system. For a magnetic HEA, the resistivity is a sum of three terms, $\rho(T) = \rho_{imp} + \rho_{ph}(T) + \rho_m(T)$, where ρ_{imp} is the residual resistivity due to elastic scattering of the electrons from impurities and from lattice defects, ρ_{ph} is the contribution due to inelastic electron-phonon scattering and ρ_m is the magnetic contribution. The microscopic mechanism of ρ_m is inelastic

scattering of the conduction electrons by the thermally-induced magnetic excitations of the magnetic state. Coupling of the magnetic excitations to the conduction electrons induces electronic transitions from an occupied state $|\vec{k}\sigma\rangle$ to an unoccupied state $|\vec{k}'\sigma'\rangle$ (where $\vec{k}$ is the wave vector and σ the spin of the conduction electron), which increases ρ_m and hence the total resistivity ρ. The ρ_m contribution is best observed in the form of magnetoresistance, $[\rho(B) - \rho(0)]/\rho(0) = \Delta\rho/\rho$. For exchange-coupled spins with parallel alignment (FM-type), the growing Zeeman interaction in an increasing external magnetic field suppresses thermally induced fluctuations of the localized 3*d* moments (it "locks" them into the field direction), resulting in a negative magnetoresistance that approaches linear variation ($\Delta\rho/\rho \propto -B$) at larger fields [16]. The same type of magnetoresistance is also observed in paramagnetic systems. For the spins aligned antiparallel (AFM-type), the fluctuations of spins on the sublattice parallel to the field are suppressed in the same way as in the paramagnetic and FM cases, whereas the fluctuations of spins on the antiparallel sublattice increase (the field tries to turn over these spins). The magnetoresistance in such a case is positive and increases as $\Delta\rho/\rho \propto B^2$ at low fields [17].

The temperature-dependent electrical resistivity $\rho(T)$ of the FCCMA in zero magnetic field is shown in Fig. C1 of the Appendix C, whereas the magnetoresistance, $\Delta\rho/\rho$, curves at selected temperatures, for the field sweep of ±9 T are shown in Fig. 8. In the upper temperature range between $T_{C1} \approx 425$ K and about 200 K, the magnetoresistance is negative in the entire field range, approaching linear variation ($\Delta\rho/\rho \propto -B$) at larger fields. The magnetoresistance slightly increases (in the absolute sense) upon lowering the temperature. Below 200 K, the shape of the $\Delta\rho/\rho$ curves changes qualitatively. In a narrow field range about the $B = 0$ origin, the magnetoresistance is positive and increases with the field (shown for the 2-K curve on an expanded scale in the inset of Fig. 8). After passing a maximum, $\Delta\rho/\rho$ decreases in a linear-like manner

($\Delta\rho/\rho \propto -B$) at still higher fields. The temperature range of this modified magnetoresistance correlates with the temperature range where the $M(H)$ hysteresis becomes significant (inset in Fig. 6b). The field-dependence of $\Delta\rho/\rho$ can be understood in analogy to the FM and AFM magnetoresistance, by considering that the magnetic structure of the FCCMA nanocomposite consists of magnetically polarized nanodomains that freeze in random directions upon zero-field cooling. When the field is applied at the measurement temperature, the domains are pinned for the external field lower than the coercive field, $B < \mu_0 H_c$. When the field exceeds the coercive field, the domains start to fluctuate in a similar way as in the AFM case (the fluctuations increase until the domains' moments start to rotate into the field direction). This results in a positive, growing magnetoresistance in a narrow field range when B just exceeds $\mu_0 H_c$ and a negative-sloping magnetoresistance $\Delta\rho/\rho \propto -B$ at higher fields $B \gg \mu_0 H_c$, where all magnetic domains are already polarized into the field direction.

3. Discussion

The presented results indicate that the magnetic state of the single-crystalline FeCoCrMnAl two-phase nanocomposite is determined by the interplay of its two constituents, the magnetic nanoplatelets of one type of magnetic order and the matrix of another, different type of magnetic order. Since in the temperature region between $T_{C1} \approx 425$ K and $T_{C2} \approx 370$ K, one of the constituents is already in a magnetically ordered state, while the other is still paramagnetic, it is possible to unravel the magnetism of each constituent separately. In the following we perform a qualitative discussion, assuming simplified chemical composition of the two constituents. The chemically disordered quinary bcc matrix, in which the Fe, Cr and Mn atoms represent 87 at. %

of all atoms, is approximated by an Fe-Cr-Mn ternary solid solution (by neglecting the presence of Al and Co, its chemical composition would be $Fe_{32}Cr_{39}Mn_{29}$). Likewise, we approximate the quinary B2 nanoplatelets, in which the Al, Co and Mn represent 80 % of all atoms, by a ternary B2 intermetallic compound $Al_{30}Co_{49}Mn_{21}$, which can also be considered as a pseudo-binary compound $Al_{30}(Co,Mn)_{70}$. For the strictly stoichiometric case $Al_{50}(Co,Mn)_{50}$, the B2 structure can be viewed as two interpenetrating cubic lattices of the CsCl type, one occupied by Al and the other by Co and Mn that randomly substitute each other. In the non-stoichiometric case, the excess Co and Mn atoms represent antistructure defects occupying Al sites on the Al sublattice.

The magnetism of the Fe-Cr-Mn alloys has been studied in the past [18,19]. Starting with the binary Fe-Cr system of bcc symmetry, it is a prototype of an alloy with a miscibility gap, which extends over a wide concentration range [18,20,21]. The Fe-Cr system shows compositional instability, where randomly disordered alloys segregate into Fe-rich and Cr-rich domains by annealing in the miscibility gap, bounded by the temperature T_M (amounting to 820 K for the 50:50 concentration). Magnetically, Fe-Cr is a system with competing FM and AFM interactions, where upon segregation, Fe-rich domains order FM, whereas Cr-rich domains order AFM. Adding Mn, the Fe-Cr-Mn alloys with near-equimolar compositions have similar structural and magnetic properties as the Fe-Cr alloys, but the magnetic transition temperature is considerably higher for the same Fe/(Fe + Cr) ratio. The $Fe_{43.5}Cr_{46.3}Mn_{10.2}$ alloy of bcc structure was reported to order FM at the transition temperature 460 K [18], quite close to the T_{C1} of the FCCMA.

The magnetism of the $Al_{1-x}Co_x$ B2-structure alloys is controlled by the amount of antistructure Co defects occupying the Al sites [22]. The stoichiometric $Al_{50}Co_{50}$ is paramagnetic, whereas in the concentration range $50.3 \leq x \leq 63$ at. % Co, a spin glass phase and growth of

magnetic clusters were observed. For x > 63 % Co, the alloys order FM. The transition temperatures depend on the thermal treatment, but magnetic ordering in the $Al_{1-x}Co_x$ generally takes place at lower temperatures than in the Fe-Cr-Mn alloys. Since Co is FM as the elemental metal, whereas Mn is AFM, the transition temperatures of the $Al_{1-x}(Co,Mn)_x$ pseudo-binary B2 alloys are expected to be lower from those of the binary $Al_{1-x}Co_x$.

Our FCCMA nanocomposite material grown by the Bridgman method was thermally annealed for several hours during slow cooling (the annealing is inherent to the Bridgman method), so that phase segregation within the predominantly Fe-Cr-Mn bcc matrix is likely. The established short-range chemical order in the form of Fe-rich FM-type clusters and Cr-Mn-rich AFM-type clusters suggests a disordered magnetic state of the matrix, analogous to magnetic metallic glasses, where asperomagnetic (predominantly FM-type disordered state) and speromagnetic (predominantly AFM-type disordered state) are frequently observed [23,24]. We associate the upper magnetic phase transition at $T_{C1} \approx 425$ K with the ordering of the matrix.

The magnetic ordering of the matrix is best observed in the temperature range between T_{C1} and T_{C2}, where the nanoplatelets are still in the paramagnetic state and hence do not perturb the matrix. The growth of the dc magnetization with the temperature below T_{C1} is of a FM-type. The peak of the ac susceptibility at T_{C1} that shifts with an increasing frequency to higher temperatures signals spin freezing dynamics of a frustrated magnet. The TRM is large and decays significantly with the time, whereas the $M(H)$ curves saturate at high fields to an inclined linear line. The magnetoresistance is negative and of $\Delta\rho/\rho \propto -B$ type. All these features suggest that the magnetic state of the matrix is asperomagnetic (ASPM). Asperomagnetism is a collective magnetic state [23,24], appearing in disordered spin systems characterized by probability distributions of the atomic moments $P(\mu)$, the exchange interactions $P(\mathcal{J})$, the magnetic anisotropy $P(D)$, and the

dipolar interactions $P(H_d)$. By assuming an exchange-dominated system, the ASPM state is characterized by a $P(\mathcal{J})$ distribution of the exchange coupling constants $\mathcal{J}$ that extends on both $\mathcal{J} > 0$ (ferromagnetic) and $\mathcal{J} < 0$ (antiferromagnetic) sides, but is biased towards a net positive value, so that the average $\bar{\mathcal{J}} > 0$. The average interaction is hence ferromagnetic and favors parallel ordering of the spins, but locally there are also magnetic domains with antiparallel ordering. Under the influence of random local easy directions that exist due to the distribution of magnetic anisotropy, the structure breaks up into randomly oriented magnetic nanodomains, the majority of which are FM-type and the minority are AFM-type. In the ASPM state, the site-averaged spin correlations $\langle \vec{S}_i(0) \cdot \vec{S}_j(r) \rangle$ are ferromagnetic and average to zero on a mesoscopic spatial scale, yielding large TRM. The $M(H)$ curves of an asperomagnet are a sum of a FM magnetization M_{FM} that saturates to a constant (horizontal plateau) and an AFM magnetization M_{AFM} that saturates to a linear, inclined line, and so does the total ASPM magnetization $M_{AS} = M_{FM} + M_{AFM}$. Due to the predominant FM magnetization component, the magnetoresistance is negative and of a FM-type. In contrast, a disordered ferromagnetic state is characterized by a $P(\mathcal{J})$ distribution that is located entirely on the $\mathcal{J} > 0$ side and the $M(H)$ curves saturate to a horizontal plateau (as there is no AFM component in the magnetization). The above described characteristic features of the ASPM and the disordered FM states are schematically summarized in Fig. 9.

Below $T_{C2} \approx 370$ K, the nanoplatelets start to order magnetically. Nanoplatelets are separated in space from each other, but are in a direct contact to the matrix. Due to the nanometric dimensions of the nanoplatelets, the portion of their surface atoms in contact to the matrix is large, so that the matrix-nanoplatelets interaction may be significant. Since at T_{C2}, the matrix is already in a magnetically ordered ASPM state, it may perturb the magnetic ordering of the nanoplatelets. Assuming that the nanoplatelets can be approximated by a pseudo-binary B2 compound

$Al_{30}(Co,Mn)_{70}$, the concentration of the Co and Mn antistructure defects occupying the Al sites on the Al sublattice is large enough that the nanoplatelets order FM. This is supported by the strongly growing FM-type magnetization below T_{C2} (Fig. 4), the FM-type $M(H)$ curves (Fig. 6a) and the FM-type magnetoresistance (Fig. 8). The strong FM magnetization of the nanoplatelets could perturb back the matrix. The basic question here is whether the coupling between the matrix and the nanoplatelets is strong enough that the magnetic state below T_{C2} is a collective state of the interacting two-phase nanocomposite system or it is so weak that the magnetic ordering of each of the two subsystems can be treated, to a good approximation, as independent down to the lowest temperatures.

The complex temperature-dependent TRM shown in Fig. 7 offers a possibility to elucidate the nature of the magnetic state of the FCCMA nanocomposite. The ultraslow TRM time-decay is a manifestation of broken ergodicity of a magnetically frustrated system, where the spin system cannot reach thermal equilibrium on the finite time scale of the employed experimental technique. By cooling the sample in a field H_{fc} to the measuring temperature T_m and stopping there for the aging time t_w before cutting the field to zero, the spin system tries to reach thermal equilibrium. The approach towards equilibrium can be phenomenologically described by a stretched-exponential function with the fc time constant τ_{fc}, so that the fc magnetization after t_w can be written as [25]

$$M_{fc}(T_m, H_{fc}, t_w) = M^{rev} + M^{TRM,0}\{1 - exp[-(t_w/\tau_{fc})^{\alpha}]\}. \quad (1)$$

Here α is the stretched exponent ($0 < \alpha < 1$), $M^{rev}(T_m, H_{fc})$ is the reversible part of the magnetization, which follows the magnetic field instantaneously, and $M^{TRM,0}(T_m, H_{fc})$ is the thermoremanent magnetization achieved after a long aging time $t_w \to \infty$. Upon cutting the field

H_{fc} to zero, the M^{rev} vanishes instantaneously, and the TRM decays slowly with a zero-field time constant τ_0 and a stretched exponent β [26]

$$M^{TRM}(T_m, H_{fc} = 0, t_w, t) = M^{TRM,0}\{1 - exp[-(t_w/\tau_{fc})^{\alpha}]\}exp[-(t/\tau_0)^{\beta}]. \quad (2)$$

$M^{TRM,0}$ is a fraction of M_{fc} prior to cutting the field to zero, with its magnitude increasing upon cooling. In the following we shall assume, for simplicity, that during aging for t_w in a field H_{fc}, the TRM has reached its full value $M^{TRM,0}$ (hence using the $t_w \to \infty$ limit of Eq. (2)), a constraint that is easy to relax.

We discuss the TRM normalized to the M_{fc} value, M^{TRM}/M_{fc}. Three characteristic temperature ranges can be defined in Fig. 7a, denoted as I, II and III. Range I is between $T_{C1} \approx$ 425 K and $T_{C2} \approx$ 370 K, where the matrix is in the ASPM state, whereas the nanoplatelets are still paramagnetic. We have

$$\frac{M^{TRM}(t)}{M_{fc}} = \frac{M_{AS}^{TRM,0}\, exp[-(t/\tau_0)^{\beta}]}{M_{AS}^{rev} + M_{AS}^{TRM,0}}. \quad (3)$$

Just below T_{C1}, the reversible part M_{AS}^{rev} of the ASPM magnetization $M_{AS} = M_{AS}^{rev} + M_{AS}^{TRM,0}$ is much larger than the TRM part, $M_{AS}^{rev} \gg M_{AS}^{TRM,0}$. Upon cooling, the TRM part grows, whereas the reversible part diminishes. As a result, the $t = 0$ amplitude $M^{TRM}(0)/M_{fc}$ increases from T_{C1} to T_{C2} and reaches a value 0.4 close to T_{C2} (Fig. 7a). The TRM time decay $M^{TRM}(t)/M_{fc}$ is strong within the range I, but slows down upon cooling from T_{C1} to T_{C2} (Fig. 7b).

Within range II between T_{C2} and about 300 K, the nanoplatelets start to order magnetically, contributing a FM component to the fc magnetization. We assume that, within this temperature range, coupling between the nanoplatelets and the matrix is still weak enough to allow treating the FM magnetization of the nanoplatelets and the ASPM magnetization of the matrix as independent. Since within range II there is still no $M(H)$ hysteresis (see inset in Fig. 6b), the FM nanoplatelets

can be assumed perfectly magnetically soft. Their magnetization is consequently fully reversible, being nonzero only in the presence of a magnetic field. This yields

$$\frac{M^{TRM}(t)}{M_{fc}} = \frac{M_{AS}^{TRM,0}\, exp\left[-(t/\tau_0)^{\beta}\right]}{M_{FM}^{rev} + M_{AS}^{rev} + M_{AS}^{TRM,0}} \,. \qquad (4)$$

Upon cooling, $M_{AS}^{TRM,0}$ still grows at the expense of M_{AS}^{rev}. However, the growth of the FM component M_{FM}^{rev} between T_{C2} and about 300 K is much stronger (Fig. 4), imposing the leading temperature dependence to M_{fc}. This results in a strong decrease of the amplitude $M^{TRM}(0)/M_{fc}$ within the range II (Fig. 7a). The TRM time decay $M^{TRM}(t)/M_{fc}$ is already very slow within this temperature range (Fig. 7b), indicating stiffening of the spin system (stronger interspin coupling) upon cooling.

Within temperature range III that extends from about 300 K down to the lowest measured temperature of 2 K, the $M(H)$ curves already saturate to a horizontal plateau (Fig. 6a) and the TRM time-decays become practically unobservable, indicating strongly interacting ("stiff") spin system. This suggests a single, collective magnetic state of the FCCMA nanocomposite, so that partitioning into the FM state of the nanoplatelets and the ASPM state of the matrix is no more appropriate. The fc magnetization is constant with the temperature (Fig. 4). The rectangular step-type $M(H)$ curves indicate a FM nature of the collective state, and we denote the magnetization of this state as $M_{FM,c}$ (with the subscript c denoting "collective"). A small $M(H)$ hysteresis appears, so that the FM magnetization of the collective state can no more be treated as perfectly magnetically soft. The FM magnetization is still a sum of the reversible and the TRM components, $M_{FM,c} = M_{FM,c}^{rev} + M_{FM,c}^{TRM}$, where, upon lowering the temperature, $M_{FM,c}^{TRM}$ increases at the expense of $M_{FM,c}^{rev}$, a consequence of the fact that the coercive field H_c increases. This yields

$$\frac{M^{TRM}(t)}{M_{fc}} = \frac{M_{FM,c}^{TRM}}{M_{FM,c}^{rev} + M_{FM,c}^{TRM}} \,, \qquad (5)$$

where the denominator is constant in temperature. Since $M_{FM,c}^{TRM}$ increases at the expense of the $M_{FM,c}^{rev}$ upon lowering the temperature, the TRM amplitude $M^{TRM}(0)/M_{fc}$ grows upon cooling within range III, as indeed observed in Fig. 7a.

The temperature dependence of the TRM can thus be explained by assuming the development of a single, collective FM-type magnetic state in the FCCMA two-phase nanocomposite upon cooling, a consequence of the exchange coupling between its two constituent phases across the phase boundaries. Another evidence of this coupling is the observed magnetic softness (recall that though the coercive field H_c is non-zero below 300 K, it is still small enough to allow classifying the FCCMA nanocomposite as a magnetically soft material). Magnetic softness/hardness of a FM material is related to the magnetic anisotropy. In magnetically anisotropic materials, the magnetic moments tend to align with an easy axis, representing an energetically favorable direction of the magnetization in the crystal lattice. The tendency of the magnetization to align with the easy axis is represented by the anisotropy energy density, of which the leading term is

$$E_a = K_1 sin^2\theta \ . \qquad (6)$$

Here K_1 is the anisotropy constant (in units Jm^{-3}), and θ is the angle between the magnetization vector $\vec{M}$ and the easy axis. In nanocomposite materials composed of magnetic nanocrystallites with different anisotropy axes, a phenomenon known as exchange averaging of bulk anisotropy arises [27] when (1) the crystallites are magnetically single-domain particles, with a crystallite dimension D much less than the Bloch domain wall width δ_w, and (2) the crystallites are exchange-coupled across the grain boundaries. Under these conditions, the effective anisotropy $\langle K \rangle$ obeys the D^6 law [27]

$$\langle K \rangle = K_1^4 D^6/\pi^6 A^3 \ , \qquad (7)$$

where $\langle K \rangle$ decreases very rapidly for the reduced crystallite dimensions D in the sub-micrometer range. Here A is the exchange stiffness, related to the Curie temperature T_C roughly as $A = k_B T_C / 2a$, where a is the lattice parameter (of a simple structure). The parameter A is related to the exchange coupling constant $\mathcal{J}$ of the exchange Hamiltonian. The coercivity scales with $\langle K \rangle$ (within the Stoner-Wohlfarth model [28], the coercive field is $H_c = 2\langle K \rangle / \mu_0 M_s$, where M_s is the saturation magnetization), so that for small enough, randomly oriented exchange-coupled nanocrystallites, H_c becomes vanishing small and the material is perfectly magnetically soft. The very small H_c shown in the inset of Fig. 6b thus supports strong exchange coupling between the matrix and the nanoplatelets and hence the existence of a single, collective FM-type magnetic state in the FCCMA two-phase nanocomposite at low temperatures.

The fact that the coercivity is non-zero at low temperatures (though very small) can be related to the fact that the nanoplatelets are magnetically not single-domain particles. The exchange length l_{ex}, which describes the shortest scale on which the magnetization can be twisted to form magnetic domains in order to minimize the dipolar interaction, is in most FM materials in the range 2–5 nm. The criterion for magnetically single-domain nanoparticles is their dimension $D \leq l_{ex}$, a condition that is not fulfilled for the FCCMA nanocomposite with much larger dimensions of the nanoplatelets. The domain walls, which are geometrically constrained in the nanoplatelets, can be very narrow, as the wall width δ_w is affected by the nanoplatelet thickness. The presence of randomly oriented magnetic domains is also supported by the positive magnetoresistance in the low magnetic field $0 < B < \mu_0 H_c$, where the maximum in $\Delta\rho/\rho$ occurs at the field that polarizes the domains into the field direction. This domain structure can be considered responsible for the incomplete exchange averaging of the anisotropy in the FCCMA nanocomposite, hence preventing the material to be ideally magnetically soft. HEAs containing

magnetic 3d transition metals Fe, Co, Ni, Cr and Mn were generally found to be soft magnetic materials with small coercivities $\mu_0 H_c$ in the range 1.4 – 23 mT [7,29-34].

4. Conclusions

The results and analysis presented in this paper unravel the magnetic ordering of a single-crystalline FeCoCrMnAl HEA that is an excellent two-phase nanocomposite magnet, formed by a bcc-B2 spinodal decomposition. The nanocomposite is composed of crystallographically oriented magnetic nanoplatelets embedded in a chemically disordered matrix of different magnetic order. Due to the single-crystalline nature of the material, there is no symmetry breaking of the surface atomic monolayer at the borders between the two phases and there are no interface regions between the nanoplatelets and the matrix. The material also does not exhibit grain structure. Under these conditions, we are observing the true intrinsic magnetism of the single-crystalline FeCoCrMnAl nanocomposite HEA.

Upon cooling, the predominantly Fe-Cr-Mn bcc matrix orders first at $T_{C1} \approx 425$ K. Due to the known compositional instability of the Fe-Cr system upon thermal annealing in the miscibility gap, phase segregation into Fe-rich and Cr-Mn-rich domains is likely. The established short-range chemical order suggests a disordered, asperomagnetic-type magnetic state of the matrix, which is well supported by the presented experiments. Below $T_{C2} \approx 370$ K, the nanoplatelets start to order in a FM-type manner. The large fraction of their surface atoms in a direct contact to the matrix suggests that the matrix-nanoplatelets exchange interaction (mediated by the conduction electrons) is significant, resulting in a formation of a single, collective FM-type magnetic state in the entire nanocomposite.

The observed collective magnetism of the two-phase spinodally decomposed single-crystalline FCCMA nanocomposite HEA is different from the magnetism observed in the two-phase eutectically decomposed polygrain nanocomposite $CoCrFeNiZr_x$ (x = 0.4 – 0.5) HEAs [35], where no collective magnetic state could be found, but each of the two phases orders independently. The multigrain microstructure with many interface regions of corrupted structural symmetry may have obscured the intrinsic magnetism of the $CoCrFeNiZr_x$ HEAs.

One of the consequences of the exchange coupling between the two constituents of the FCCMA nanocomposite is a very good magnetic softness of the material. The two successive magnetic phase transitions at $T_{C1} \approx 425$ K and $T_{C2} \approx 370$ K imply that the temperature change of the magnetization $\partial M/\partial T$ is strong in a large temperature interval from 425 to 300 K, thus over the interval of about $\Delta T \approx 125$ K just above room temperature (see Fig. 4). The magnetic softness (required to minimize losses in ac applications where the material is periodically magnetized and demagnetized) and the large $\partial M/\partial T$ in a large temperature interval above 300 K are both advantageous for magnetocaloric refrigeration. The magnetocaloric effect (the adiabatic change in temperature of a magnetic system around temperature T, when exposing the material to a changing magnetic field) is enhanced in materials with large changes of the magnetization vs. temperature, at constant magnetic field. This usually happens in the vicinity of a FM phase transition. The two consequent FM-like phase transitions in the FCCMA nanocomposite make the large $\partial M/\partial T$ to be spread over a wide temperature interval, indicating that the FCCMA material is promising for magnetocaloric application in a wide temperature interval just above room temperature.

Declaration of competing interest

The authors declare that they have no known competing financial interests or personal relationships that could have appeared to influence the work reported in this paper.

CRediT authorship contribution statement

M. Krnel, S. Vrtnik, P. Koželj, Z. Jagličić: investigation, magnetic and electrical measurements.

A. Jelen: investigation, electron microscopy measurements.

A. Meden: investigation, X-ray diffraction study.

M. Feuerbacher: alloy synthesis, supervision.

J. Dolinšek: writing the manuscript, supervision.

Acknowledgments

Slovenian authors acknowledge the financial support from the Slovenian Research Agency (research core funding No. P1-0125). MF acknowledges financial support from the German Research Foundation (DFG) under grant No. FE 571/4 within the priority program SPP2006 "Compositionally Complex Alloys – High Entropy Alloys (CCA-HEA)".

Appendix A: Experimental section

The SEM imaging was performed with an FEI Helios NanoLab 650 FIB instrument. The surfaces were prepared *in-situ* by gallium ion sputtering. For the imaging, relatively low-energy electron beams were used (1 and 2 kV), in combination with in-lens secondary electron detector. The bcc

matrix and the B2 phase are nicely distinguished, most probably due to magnetic type II contrast (originating from deflection of the beam electrons by internal magnetic fields).

The high-angle annular dark field (HAADF) STEM micrographs, the EDS elemental maps and the concentration line profile were obtained by a Cs-corrected Jeol ARM 200 CF STEM microscope equipped with an SDD Jeol Centurio energy-dispersive X-ray spectrometer (EDS). The operating voltage was set to 200 kV. A Gatan Quantum ER Dual EELS system was used for EELS spectra collection and sample thickness estimation. The HAADF images were taken with 68 mrad inner and 175 mrad outer semiangles and convergence angle of 24 mrads.

The sample for the STEM analysis was prepared using a tripod polishing method (Multiprep polishing system from Allied), where the sample was first mechanically thinned to a few micrometers and finally thinned down to electron transparency using a Gatan PIPS II ion-milling system. During this step, the sample was cooled with liquid nitrogen. The final sample thickness in the analyzed areas was about 10 nm.

Magnetic measurements were conducted by a Quantum Design MPMS3 SQUID magnetometer equipped with a 7-T magnet, operating at temperatures between 1.8 and 1000 K. The sample for measurements was needle-shaped, with the long dimension of 4 mm and the perpendicular dimension of 0.5 mm. The long dimension was set in the direction of the external magnetic field. Due to rounded edges, the shape of the sample resembled a rotational ellipsoid, for which the demagnetization effects are minimized.

Electrical resistivity and magnetoresistance measurements were performed by a Quantum Design Physical Property Measurement System PPMS 9T. A rectangular-bar sample of dimensions $1\times1\times8$ mm^3 was used, with the long dimension oriented along the field direction to minimize the demagnetization effects.

Appendix B: Three-dimensional morphology of the FCCMA nanocomposite

The three-dimensional platelet-type morphology of the inclusions is confirmed by SEM SE images of Fig. B1, where the primary and the perpendicular surfaces are shown. Both surfaces were prepared by cutting and polishing with a gallium ion beam in an FIB instrument.

Appendix C: Electrical resistivity

The temperature-dependent electrical resistivity $\rho(T)$ of the FCCMA in zero magnetic field is shown in Fig. C1. The impurity contribution (ρ_{imp}) due to elastic scattering of the electrons from impurities and from lattice defects results in a large magnitude of the resistivity and its small total variation in the investigated temperature range 400 – 2 K. The inelastic electron-phonon scattering contribution (ρ_{ph}) is responsible for the positive temperature coefficient of the resistivity. The magnetic contribution ρ_m is best observed in the form of magnetoresistance, shown in Fig. 8.

Table 1. Binary mixing enthalpies (in $kJmol^{-1}$) for unlike atom pairs constituting the FeCoCrMnAl HEA [12].

Fe	–1	–1	0	–11
–1	Co	–4	–5	–19
–1	–4	Cr	2	–10
0	–5	2	Mn	–19
–11	–19	–10	–19	Al

References

[1] J.M.D. Coey, Magnetism and Magnetic Materials, Cambridge University Press, Cambridge, 2010, Ch. 8, pp. 264–299.

[2] H. Liang, J.W. Miao, B.Y. Gao, D.W. Deng, T.M. Wang, Y.P. Lu, Z.Q. Cao, H. Jiang, T.J. Li, H.J. Kang, Surf. Coat. Technol. 400 (2020) 13.

[3] D. Chung, Z.Y. Ding, Y. Yang, Adv. Eng. Mater. 21 (2019) 11.

[4] J. Brechtl, S. Chen, C. Lee, Y. Shi, R. Feng, X. Xie, D. Hamblin, A.M. Coleman, B. Straka, H. Shortt, R.J. Spurling, P.K. Liaw, Metals 10 (2020) 1101.

[5] Y. Zhang, T.T. Zuo, Z. Tang, M.C. Gao, K.A. Dahmen, P.K. Liaw, Z.P. Lu, Prog. Mater. Sci. 61 (2014) 1.

[6] L.J. Santodonato, Y. Zhang, M. Feygenson, C.M. Parish, M.C. Gao, R.J.K. Weber, J.C. Neuefeind, Z. Tang, and P.K. Liaw, Nat. Commun. 6 (2015) 5964.

[7] P. Koželj, S. Vrtnik, A. Jelen, M. Krnel, D. Gačnik, G. Dražić, A. Meden, M. Wencka, D. Jezeršek, J. Leskovec, S. Maiti, W. Steurer, and J. Dolinšek, Adv. Eng. Mater. (2019) 1801055. DOI: 10.1002/adem.201801055.

[8] S. Maiti, W. Steurer, Acta Mater. 106 (2016) 87.

[9] S. Vrtnik, P. Koželj, A. Meden, S. Maiti, W. Steurer, M. Feuerbacher, J. Dolinšek, J. Alloys Compd. 695 (2017) 3530.

[10] M. Feuerbacher, E. Würtz, A. Kovács, C. Thomas, Mat. Res. Lett. 5 (2017) 128.

[11] A. Manzoni, H. Daoud, R. Völkl, U. Glatzel, N. Wanderka, Ultramicroscopy 132 (2013) 212.

[12] F.R. de Boer, R. Boom, W.C.M. Mattens, A.R. Miedema, A.K. Niessen, Cohesion in Metals: Transition Metal Alloys (Cohesion and Structure), North Holland, Amsterdam, 1988.

[13] J.A. Mydosh, Spin Glasses: An Experimental Introduction, Taylor & Francis, London, 1993, p. 67.

[14] M. Lederman, R. Orbach, J.M. Hammann, M. Ocio, E. Vincent, Phys. Rev. B 44 (1991) 7403.

[15] D. Chu, G.G. Kenning, R. Orbach, Phil. Mag. B 71 (1995) 479.

[16] H. Yamada, S. Takada, Prog. Theor. Phys. 48 (1972) 1828.

[17] H. Yamada, S. Takada, J. Phys. Soc. Jpn. 34 (1973) 51.

[18] T. Schneider, M. Acet, E.F. Wassermann, W. Pepperhoff, J. Appl. Phys. 70 (1991) 6559.

[19] W.M. Xu, P. Zheng, Z.J. Chen, B.G. Shen, J. Magn. Magn. Mater. 172 (1997) 183.

[20] M. Furusaka, Y. Ishikawa, S. Yamaguchi, J. Phys. Soc. Jpn. 55 (1986) 2253.

[21] S. Katano, M. Iizumi, Phys. Rev. Lett. 52 (1984) 835.

[22] R. Laiho, K. Eftimova, E. Lähderanta, E. Hiltunen, Solid State Commun. 87 (1993) 255.

[23] J.M.D. Coey, Magnetism and Magnetic Materials (ref. [1]), pp. 209–218.

[24] R.C. O'Handley, Modern Magnetic Materials: Principles and Applications, Wiley, New York, 1999, pp 391–410.

[25] R.V. Chamberlin, G. Mazurkevich, R. Orbach, Phys. Rev. Lett. 52 (1984) 867.

[26] J. Dolinšek, Z. Jagličić, M.A. Chernikov, I.R. Fisher, P.C. Canfield, Phys. Rev. B 64 (2001) 224209.

[27] J.M.D. Coey, Magnetism and Magnetic Materials (ref. [1]), p. 300.

[28] E.C. Stoner, E.P. Wohlfarth, Phil. Trans. Roy. Soc. London A 240 (1948), 599.

[29] M.H. Tsai, Entropy 15 (2013) 5338.

[30] See, for a review, B.S. Murthy, J.W. Yeh, S. Ranganathan, High-Entropy Alloys, Elsevier, Amsterdam, 2014, pp. 154-155.

[31] See, for a review, J.W. Yeh, S.K. Chen, H C. Shih, Y. Zhang, T.T. Zuo, in High-Entropy Alloys: Fundamentals and Applications, M.C. Gao, J.W. Yeh, P.K. Liaw, Y. Zhang (Eds.), Springer International Publishing Switzerland, 2016, pp. 243-248.

[32] M.C. Gao, D.B. Miracle, D. Maurice, X. Yan, Y. Zhang, J.A. Hawk, J. Mater. Res. 33 (2018) 3138.

[33] C. Jung, K. Kang, A. Marshal, K.G. Pradeep, J.-B. Seol, H.M. Lee, P.-P. Choi, Acta Mater. 171 (2019 31.

[34] R.-F. Zhao, B. Ren, G.-P. Zhang, Z.-X. Liu, B. Cai, J.-J. Zhang, J. Magn. Magn. Mater. 491 (2019) 165574.

[35] S. Vrtnik, S. Guo, S. Sheikh, A. Jelen, P. Koželj, J. Luzar, A. Kocjan, Z. Jagličić, A. Meden, H. Guim, H.J. Kim, J. Dolinšek, Intermetallics 93 (2018) 122.

Figure captions

Fig. 1. SEM SE image of the spinodally decomposed FeCoCrMnAl HEA, collected at 1 kV.

Fig. 2. HAADF STEM micrograph and EDS elemental maps of the spinodally decomposed FeCoCrMnAl HEA.

Fig. 3. EDS compositional line profile along the yellow line drawn in the left panel.

Fig. 4. Temperature-dependent zfc and fc dc magnetizations in a magnetic field $B = 10$ mT.

Fig. 5. (a) Real part of the ac susceptibility χ' in the temperature range 300 – 500 K. **(b)** The peak in χ' at the upper phase transition ($T_{C1} \approx 425$ K) on an expanded scale. The inset shows the $T_f(\nu)/T_f(1\text{ Hz})$ relation, where $T_f(\nu)$ is the spin freezing temperature, determined from the highest point of the χ' peak.

Fig. 6. (a) Magnetization versus magnetic field, $M(H)$, between 420 and 2 K. The inset shows the high-field parts of the curves (4–7 T), normalized to their values at 7 T, $M(H)/M(7\text{ T})$, demonstrating a decrease of the inclination of the saturation magnetization line upon cooling. **(b)** Hysteresis of the curves at 100 K and 2 K on an expanded scale. The temperature-dependent coercive field $\mu_0 H_c$ is shown in the inset.

Fig. 7. (a) Temperature-dependent TRM amplitude at the beginning of the time-decay ($t = 0$), normalized to the fc magnetization prior to cutting the field to zero, $M_{TRM}(0)/M_{fc}$. **(b)** The normalized $M_{TRM}(t)/M_{TRM}(0)$ time-decay curves at a selected set of measuring temperatures T_m.

Fig. 8. Magnetoresistance curves, $\Delta\rho/\rho$, at selected temperatures. The inset shows the 2-K curve on an expanded scale around $B = 0$. Vertical arrows mark the value of the coercive field $\pm\,\mu_0 H_c$ at $T = 2$ K.

Fig. 9. Schematic presentation of the magnetic state based on the distribution function of the exchange interactions $P(\mathcal{J})$ and the corresponding $M(H)$ magnetization curve: **(a)** disordered ferromagnetism, **(b)** asperomagnetism.

Fig. B1. SEM SE images collected at 2 kV of **(a)** the primary surface and **(b)** the surface perpendicular to it (machined by a gallium beam in an FIB instrument), confirming the three-dimensional platelet-type morphology of the inclusions.

Fig. C1. Temperature-dependent electrical resistivity $\rho(T)$ in zero magnetic field.

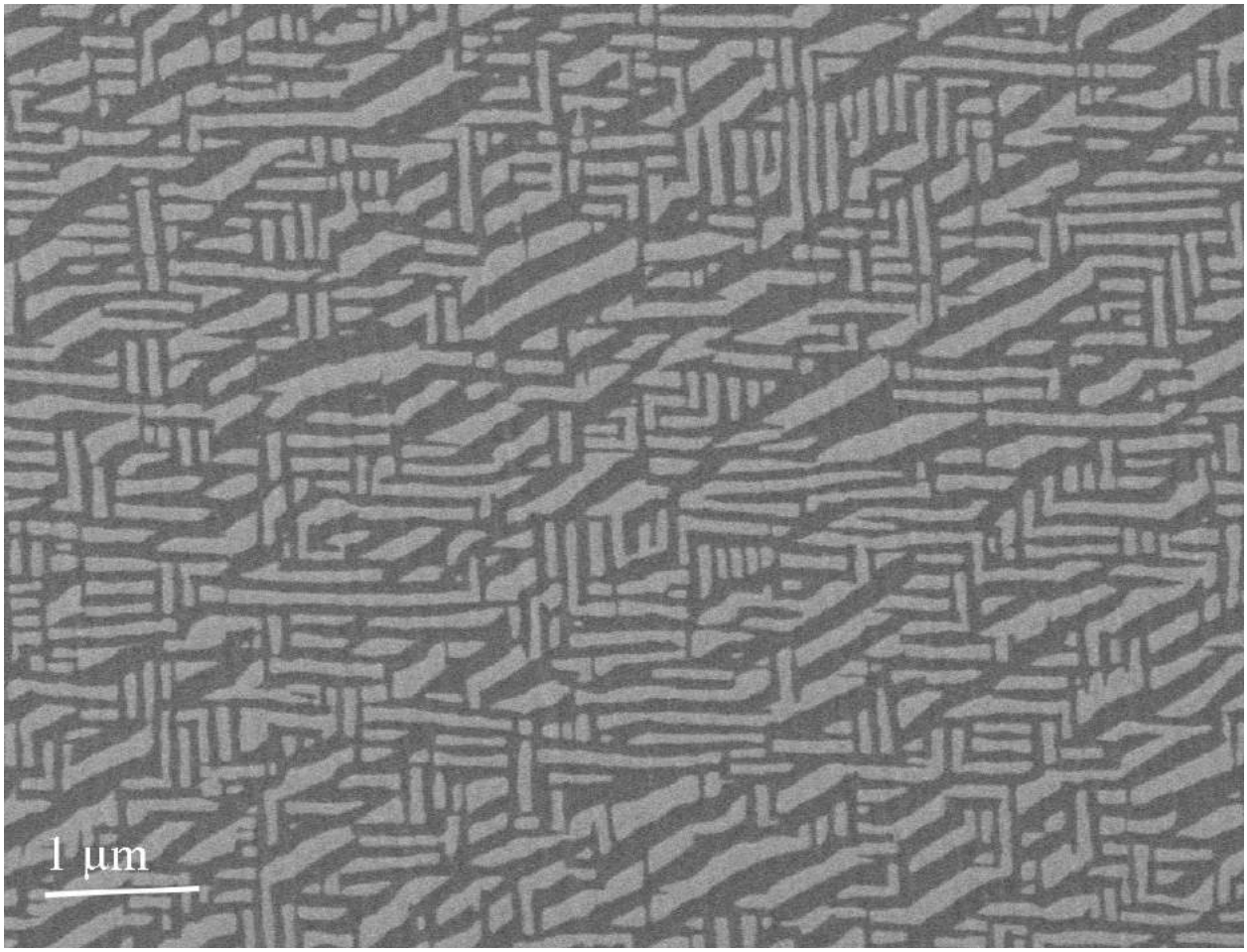

Fig. 1

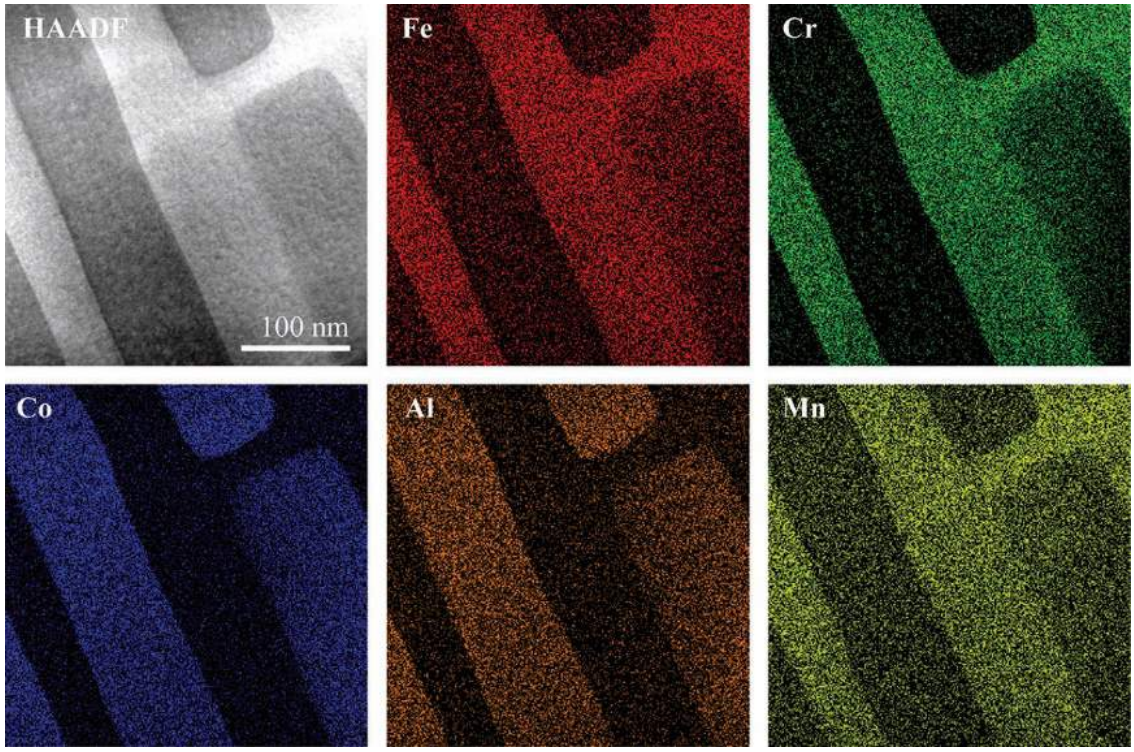

Fig. 2

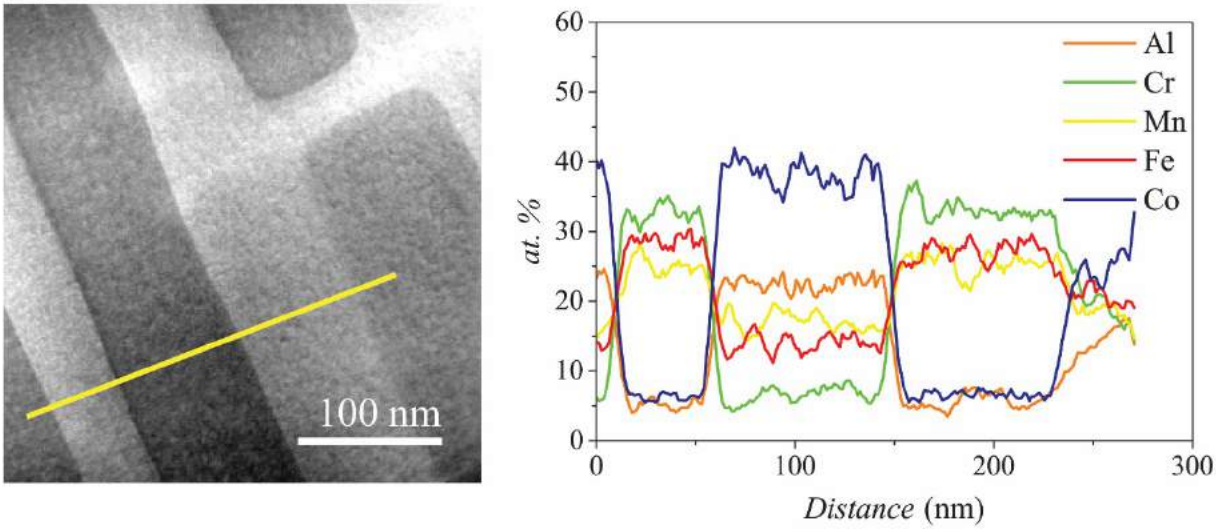
100 nm
60
50
40
30
20
10
0
at. %
0
100
200
300
Distance (nm)
Al
Cr
Mn
Fe
Co

Fig. 3

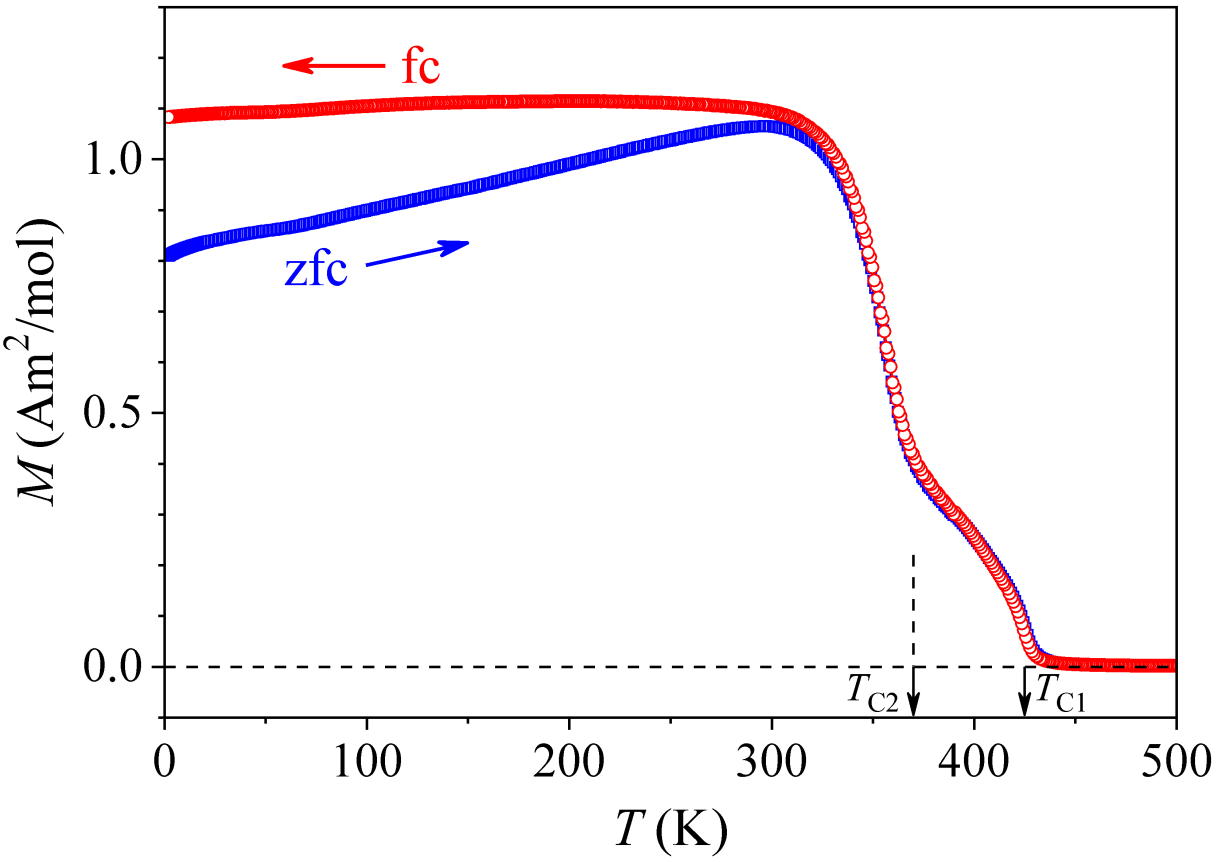

Fig. 4

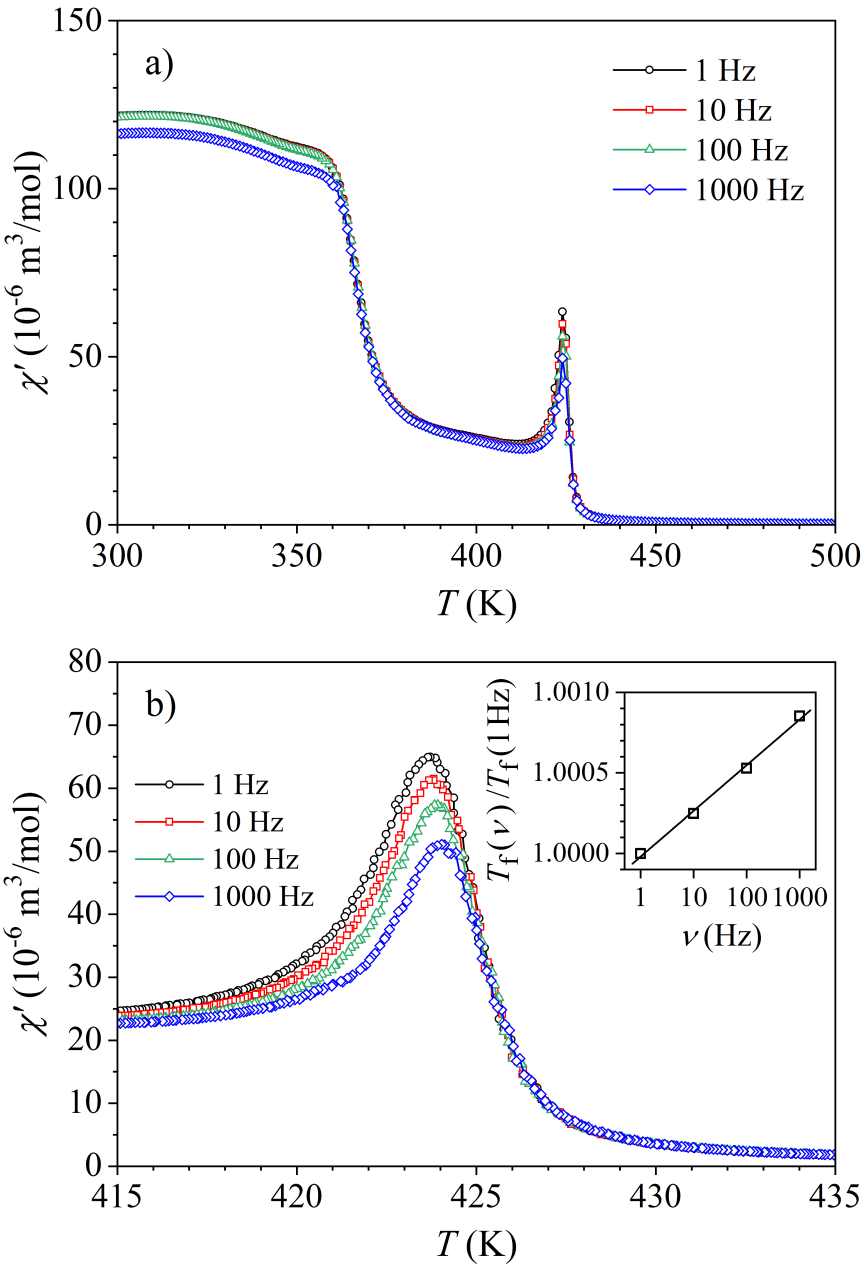

Fig. 5

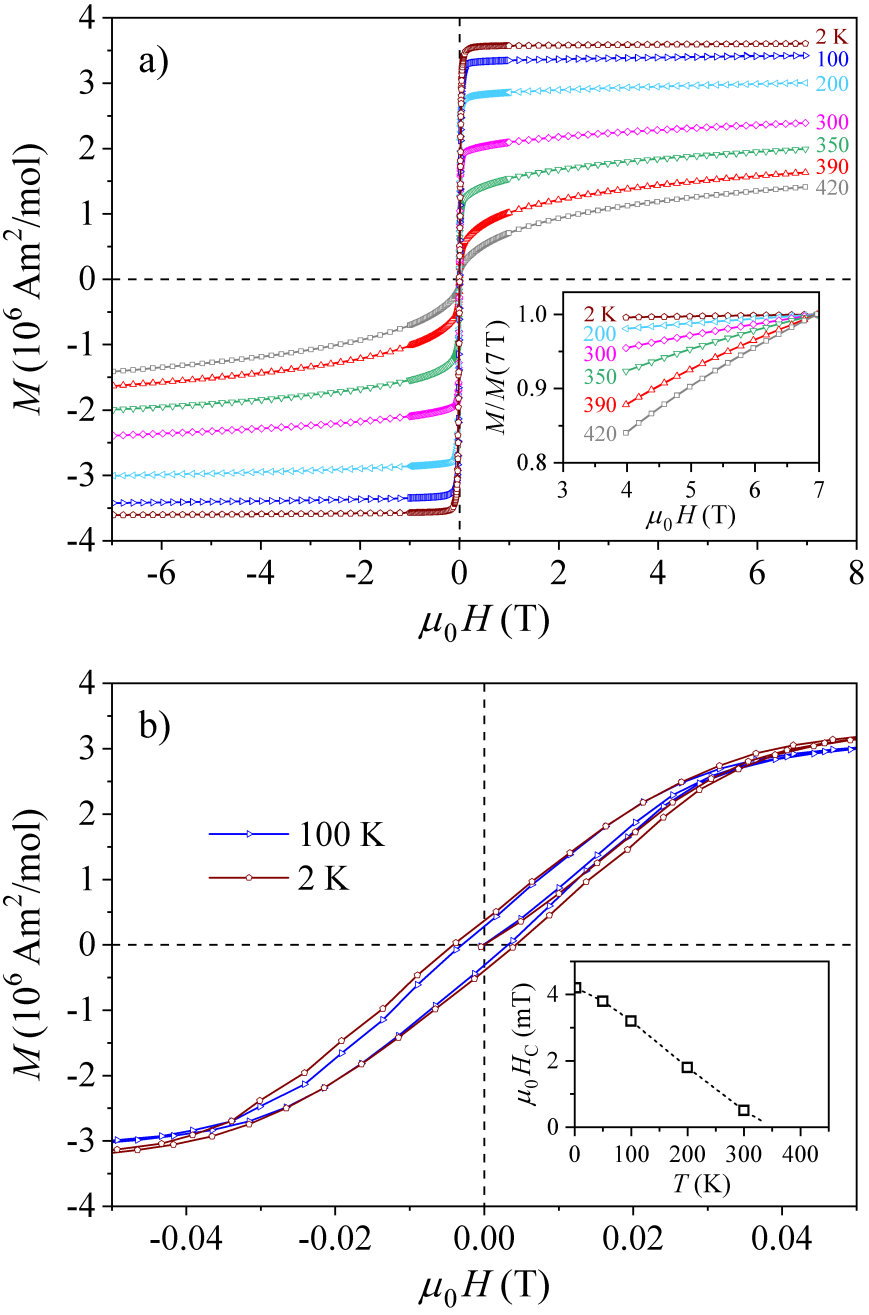
a)
2 K
100
200
300
350
390
420
M (10^6 Am^2/mol)
$\mu_0 H$ (T)
M/M(7 T)
b)
100 K
2 K
$\mu_0 H_C$ (mT)
T (K)

Fig. 6

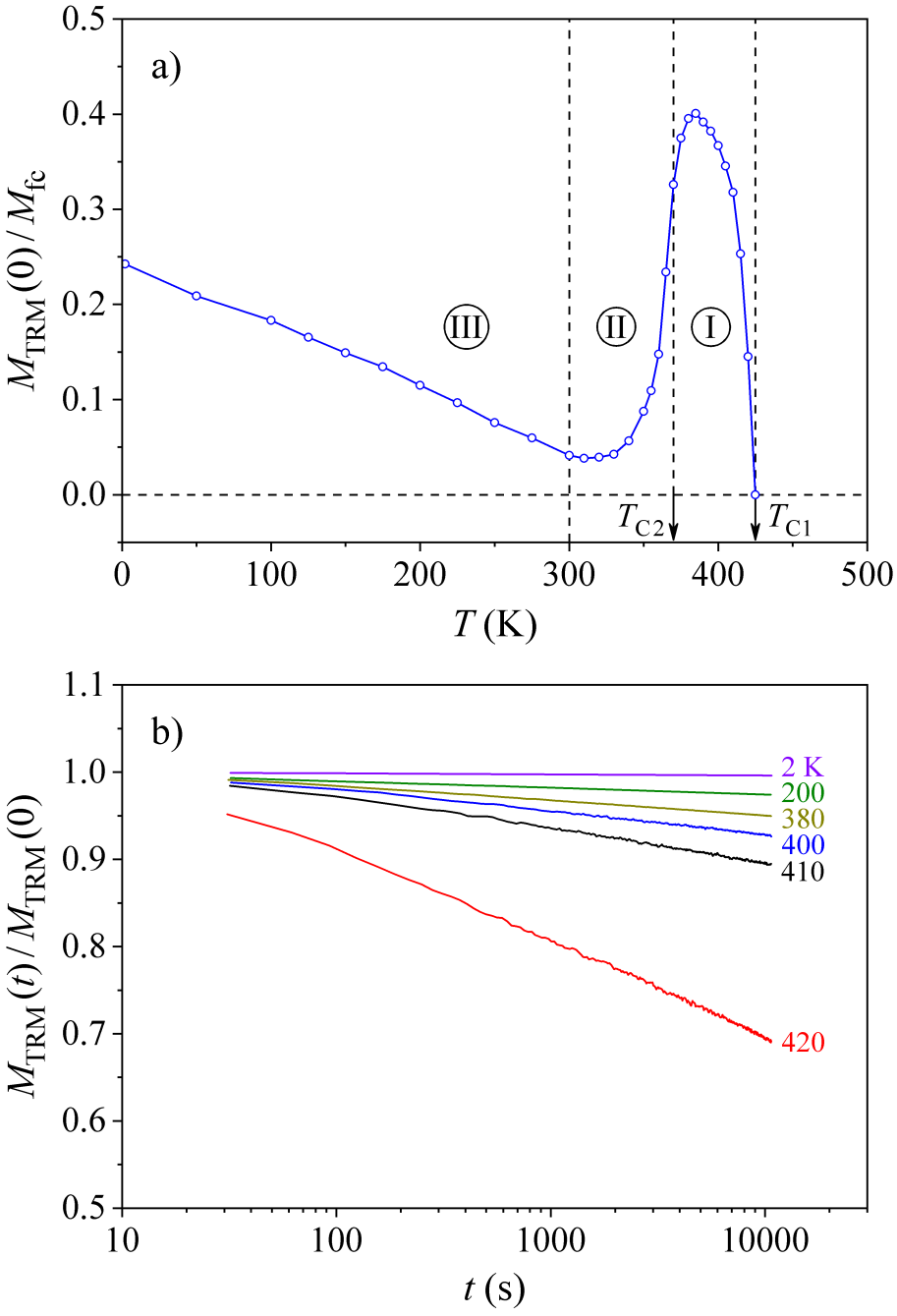
a)
$M_{TRM}(0)/M_{fc}$
III
II
I
T_{C2}
T_{C1}
T (K)
b)
$M_{TRM}(t)/M_{TRM}(0)$
2 K
200
380
400
410
420
t (s)

Fig. 7

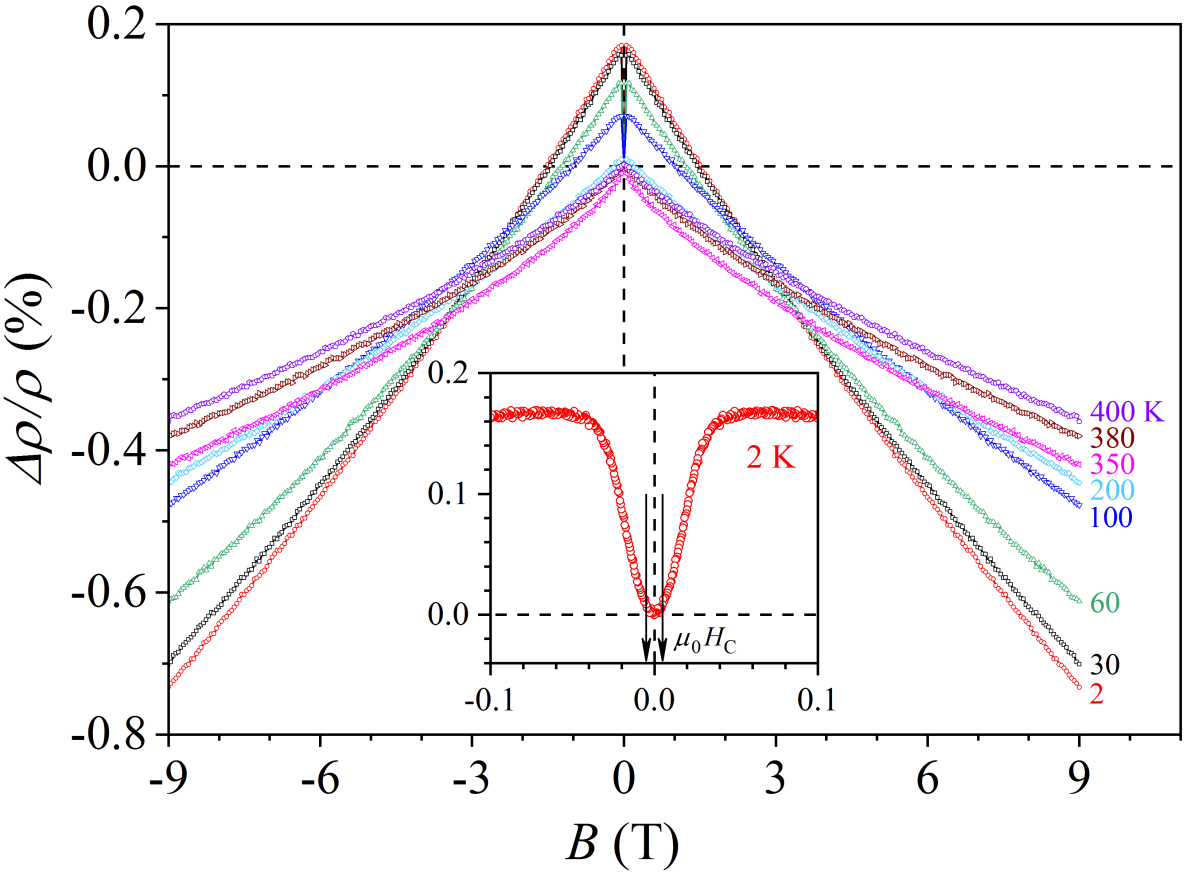
0.2
0.0
-0.2
-0.4
-0.6
-0.8
Δρ/ρ (%)
-9
-6
-3
0
3
6
9
B (T)
400 K
380
350
200
100
60
30
2
2 K
μ0HC
0.2
0.1
0.0
-0.1
0.0
0.1

Fig. 8

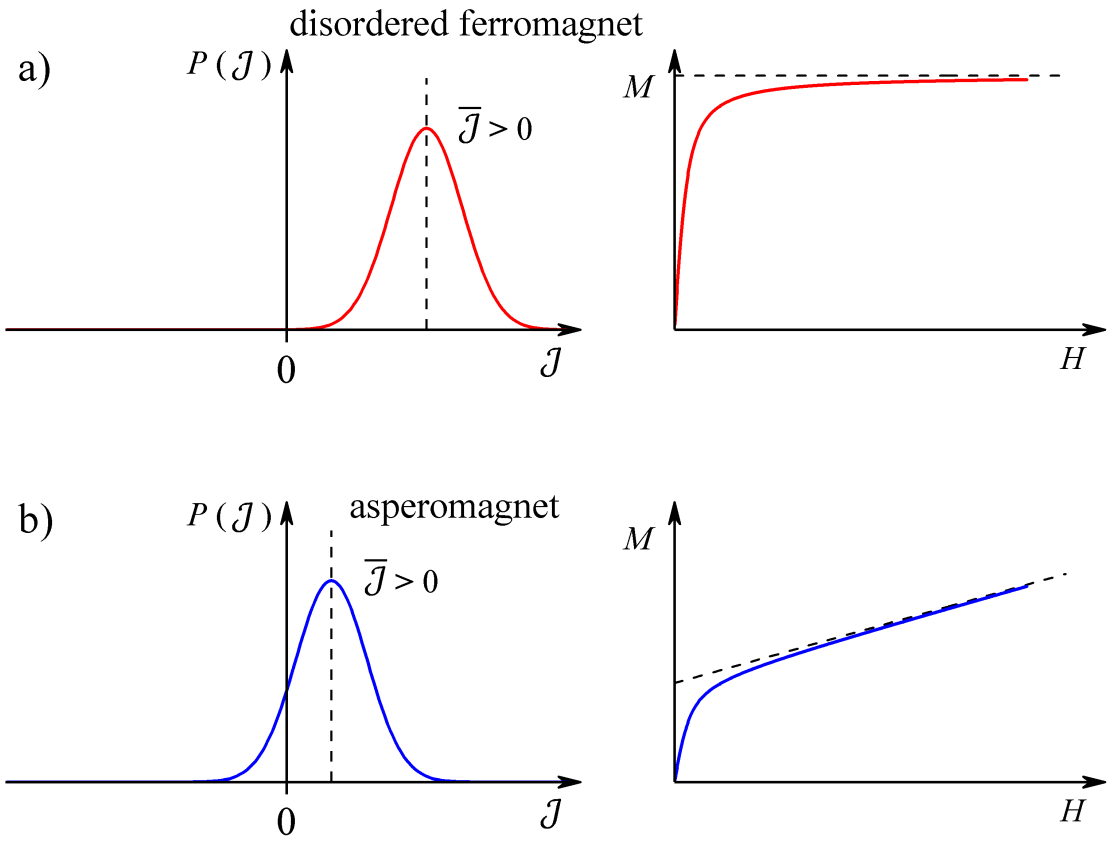
a)
disordered ferromagnet
P (J)
$\overline{J} > 0$
0
J
M
H
b)
asperomagnet
P (J)
$\overline{J} > 0$
0
J
M
H

Fig. 9

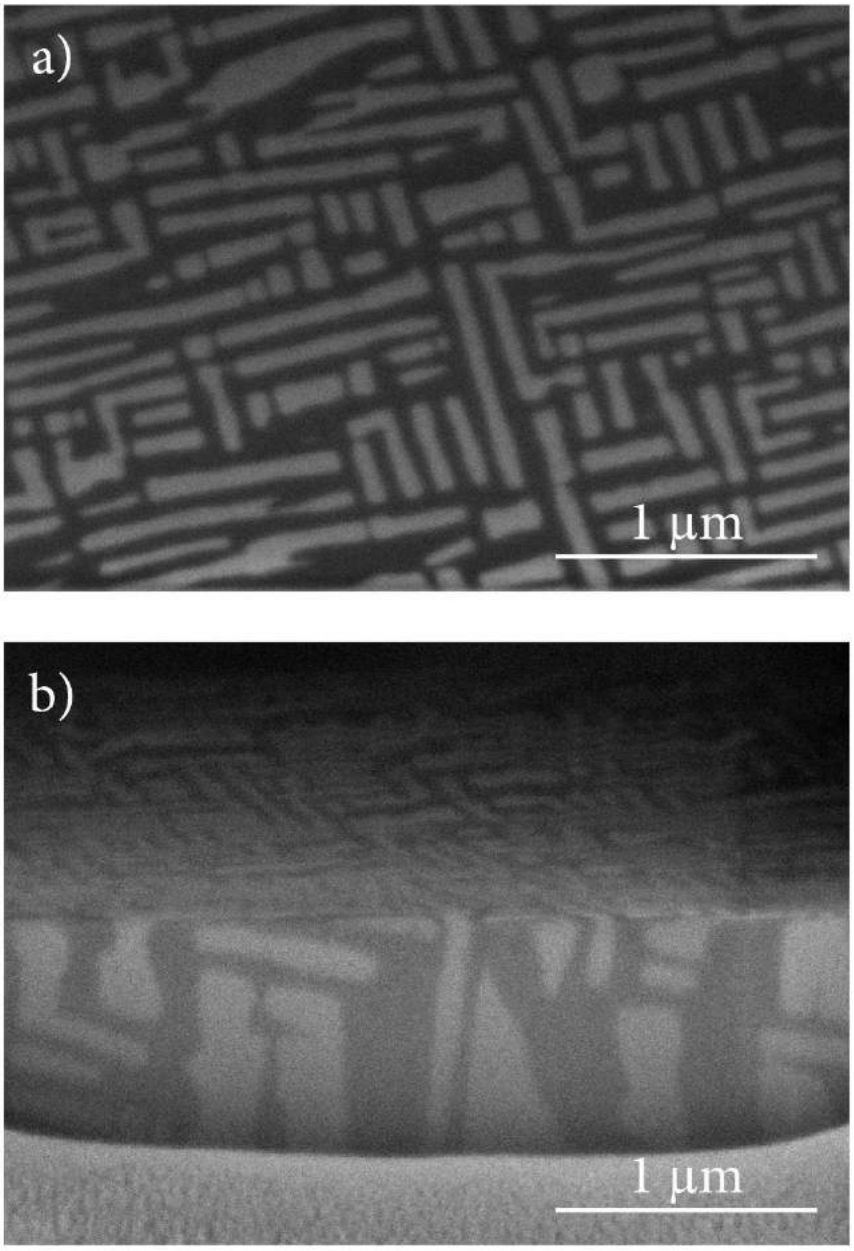

Fig. B1

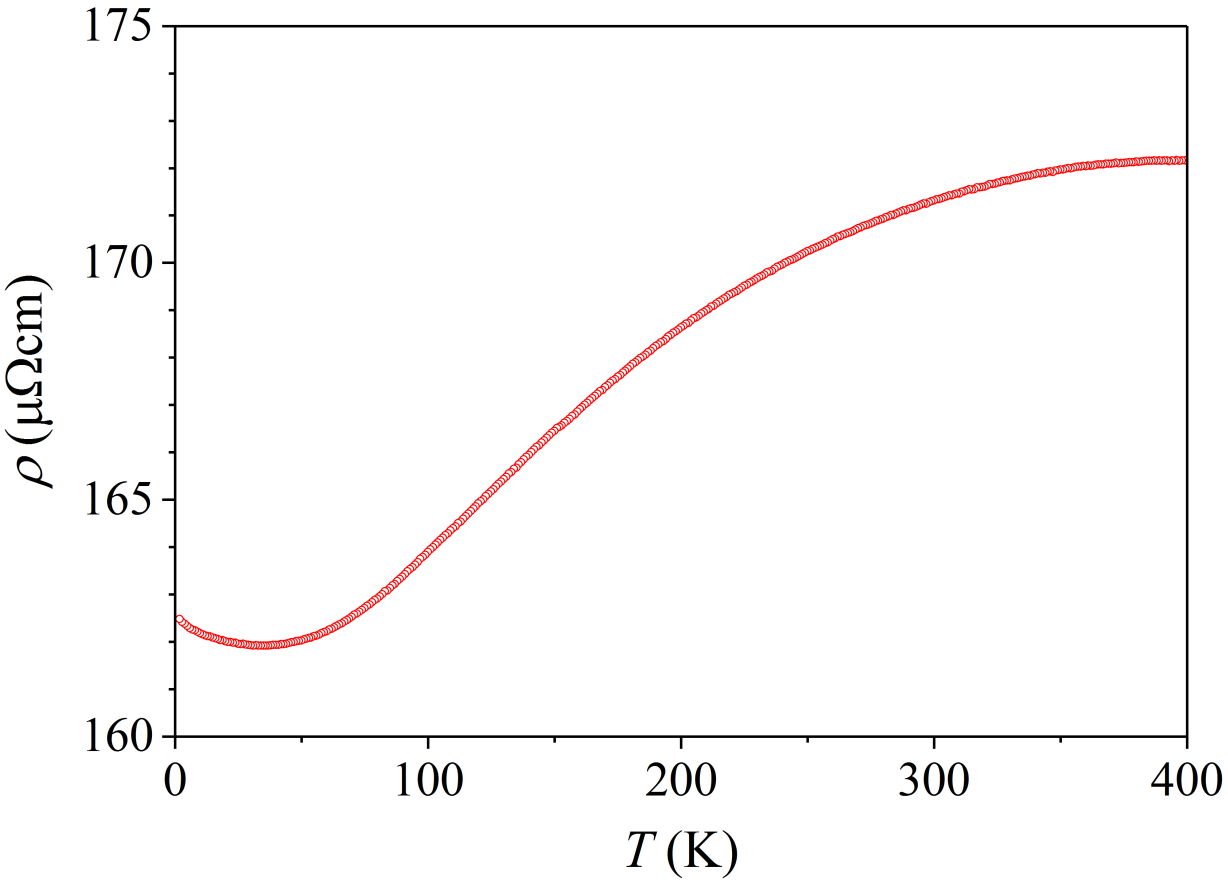

Fig. C1